Acta Crystallographica Section A
Foundations of Crystallography
ISSN 0108-7673

Received 23 January 2008
Accepted 8 March 2008

Dynamical calculation for X-ray 24-beam diffraction in a two-plate crystal cavity of silicon

M.-S. Chiu,[a] Yu. P. Stetsko[b] and S.-L. Chang[a]*

[a]Department of Physics, National Tsing Hua University, Taiwan, and [b]National Synchrotron Radiation Research Center, Hsinchu 300, Taiwan. Correspondence e-mail: slchang@phys.nthu.edu.tw

The X-ray back diffraction of (1240) in a monolithic two-plate silicon cavity occurs at photon energy 14.4388 keV, at which 24 beams are simultaneously excited. Based on the dynamical theory of X-ray diffraction, a theoretical approach has been developed for solving the fundamental equation of dynamical theory to investigate this back diffraction and the interference patterns generated by the Fabry–Perot-type resonance that produces intensity undulation in both transmitted and back-reflected beams. The section of dispersion surface and its associated linear absorption coefficients, wavefield intensities and excitation of mode are calculated. The calculated intensity distribution of the transmitted beam is in a good agreement with the observed one. Details about the interaction between the multiply diffracted X-rays and cavity resonant photons are also reported. Procedures of computer programming are also provided.

1. Introduction

An optical Fabry–Perot cavity, one of the key components of making a conventional laser, is mainly composed of two mirrors separated by a distance and nearly parallel to one another. A variety of cavities has also been proposed to guide X-rays in a close loop to generate resonance interference (Bond *et al.* 1967; Deslattes *et al.* 1968). The simplest X-ray cavity, similar to the optical Fabry–Perot cavity, is made up of a pair of crystal plates acting as reflecting mirrors. Different from the optical Fabry–Perot cavity, an X-ray Fabry–Perot cavity employs successive Bragg back diffraction from atomic planes whose Bragg angle is extremely close to 90° to confine the radiation between two crystal plates. The coherent forward- and backward-reflected X-rays from the two plates interfere with each other to generate resonance fringes. Since the idea of the X-ray Fabry–Perot cavity was proposed, there have been many theoretical studies on X-ray back diffraction (Caticha & Caticha-Ellis, 1982; Colella & Luccio, 1984; Kushnir & Suvorov, 1990; Shvyd'ko *et al.*, 1998) and X-ray Fabry–Perot interferometers (Steyerl & Steinhauser, 1979; Caticha & Caticha-Ellis, 1990; Kohn *et al.*, 2000) reported in the literature. With the advent of synchrotron radiation, a diversity of experiments has been attempted to observe the X-ray cavity resonance fringes (Liss *et al.*, 2000; Shvyd'ko *et al.*, 2003). Until recent experiments (Chang *et al.*, 2005, 2006), the resonance fringes in two-dimensional intensity distributions through angular scans were clearly observed in X-ray cavities made up of a monolithic two-plate or multiplate silicon crystal employing back diffraction of (1240) at photon energy 14.4388 keV at which 24 beams are simultaneously excited due to the crystal symmetry. The experimental conditions for detecting well resolved resonance fringes in such diffraction experiments were also discussed (Chang *et al.*, 2005, 2006).

Until now, the dynamical simulation of resonance fringes for 24-beam diffraction occurring in an X-ray Fabry–Perot cavity has not yet been reported in detail. Although Sutter *et al.* (2001) had observed the 24-beam diffraction involving the back diffraction of (1240) from a 3.8 mm thick silicon crystal plate, only a few discrete intensity scans of back diffraction (1240) over two orthogonal directions were given and the corresponding dynamically simulated curves and an image showing 10-beam diffraction spots were reported. The fully two dimensional intensity map of back diffraction (1240), the section of dispersion surface, linear absorption coefficients and excitation of mode were not mentioned.

Based on the above facts, we continue to go further to develop a theoretical approach to solve the fundamental equation of wavefield and give a better insight into the resonance fringes involving 24-beam diffraction in the X-ray Fabry–Perot cavity experiments. The section of dispersion surface, linear absorption coefficients and excitation of mode are also reported.

2. Theoretical considerations

The dynamical theory of X-ray diffraction, describing the interaction of X-rays with crystalline material, originated with Darwin (1914) and Ewald (1916), and was reformulated by von Laue (1931), taking into account multiple diffraction. A very comprehensive review can be found in the recent book by

Authier (2001). We follow von Laue's approach to give a brief review on how to obtain the fundamental equation of wavefields. The dielectric constant in crystalline materials is considered as a periodic function of space and Maxwell's equations are used to deal with the interaction of X-rays with the crystal. The solutions to Maxwell's equations, the electromagnetic fields, $\mathbf{D}(r)$, $\mathbf{E}(r)$, $\mathbf{B}(r)$ and $\mathbf{H}(r)$, in the crystal satisfying Bragg's law, are Bloch waves, which are expressed as a superposition of an infinite number of plane waves. Inserting the Bloch waves into Maxwell's equations and equating each Fourier component between two sides of equality lead to the two relations $\mathbf{K}_{\mathbf{h}_m} \times \mathbf{E}_{\mathbf{h}_m} = \nu\mu_0 \mathbf{H}_{\mathbf{h}_m}$ and $\mathbf{K}_{\mathbf{h}_m} \times \mathbf{H}_{\mathbf{h}_m} = -\nu \mathbf{D}_{\mathbf{h}_m}$, where $\mathbf{h}_m$ is the reciprocal-lattice vector involved in the diffraction, ν is the frequency and μ_0 is the permeability of the free space. The dielectric constant is defined as $\kappa = \varepsilon(r)/\varepsilon_0 = 1 + \chi$, where $\varepsilon(r)$ is the permittivity of the dielectric, ε_0 is the permittivity of free space and χ is the dielectric susceptibility. All can be expressed as a Fourier series due to the periodic nature of the crystal. Employing the relation $\mathbf{D}(r) = \varepsilon(r)\mathbf{E}(r)$, inserting the Fourier series of $\mathbf{D}(r)$, $\mathbf{E}(r)$ and $\varepsilon(r)$ into this relation and equating each Fourier component between two sides of this relation result in the equation

$$\mathbf{D}_{\mathbf{h}_m} = \varepsilon_0 \left(\mathbf{E}_{\mathbf{h}_m} + \sum_{n=0}^{N-1} \chi_{h_m - h_n} \mathbf{E}_{\mathbf{h}_n} \right) \tag{1}$$

for N diffracted waves. Finally, taking the cross product of $\mathbf{K}_{\mathbf{h}_m}$ with two sides of the relation $\mathbf{K}_{\mathbf{h}_m} \times \mathbf{E}_{\mathbf{h}_m} = \nu\mu_0 \mathbf{H}_{\mathbf{h}_m}$, the fundamental equation of wavefield is derived as follows:

$$(\mathbf{K}_{\mathbf{h}_m} \cdot \mathbf{K}_{\mathbf{h}_m} - k^2)\mathbf{E}_{\mathbf{h}_m} = (\mathbf{K}_{\mathbf{h}_m} \cdot \mathbf{E}_{\mathbf{h}_m})\mathbf{K}_{\mathbf{h}_m} + k^2 \sum_{n=0}^{N-1} \chi_{\mathbf{h}_m - \mathbf{h}_n} \mathbf{E}_{\mathbf{h}_n}, \tag{2}$$

where $m = 0, 1, \ldots, N-1$. k is the inverse of the wavelength of the incident beam. $\mathbf{K}_{\mathbf{h}_m}$ are the wavevectors participating in diffraction within the crystal, $\chi_{\mathbf{h}_m - \mathbf{h}_n}$ is the dielectric susceptibility of the crystal for the $\mathbf{h}_m - \mathbf{h}_n$ reflection. These N waves coherently couple with one another *via* the corresponding susceptibilities.

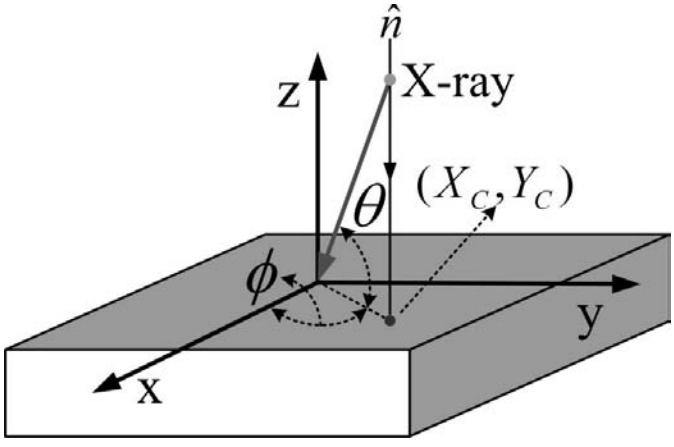

Figure 1
Cartesian coordinate frame.

To tackle such an N-beam diffraction situation in a single crystal, Stetsko & Chang (1997) introduced a Cartesian coordinate frame to decompose the electric fields and wavevectors of the fundamental equation (2) into their x, y and z components. Through matrix manipulation, the fundamental equation (2) is expressed in an eigenvalue equation of a matrix form (3). The detailed derivation was given by Stetsko & Chang (1997). The final eigenvalue equations are as follows.

$$(Q - zI_4)E_4 = 0 \tag{3}$$

$$Q = \begin{pmatrix} C & 0 & AG^{-1}A - I & AG^{-1}B \\ 0 & C & BG^{-1}A & BG^{-1}B - I \\ B^2 - G & -AB & C & 0 \\ -AB & A^2 - G & 0 & C \end{pmatrix} \tag{4}$$

$$E_4 = \begin{pmatrix} E_x \\ E_y \\ E_v \\ E_w \end{pmatrix}. \tag{5}$$

$E_x = (E_0^x, E_1^x, \ldots, E_{N-1}^x)^T$, $E_y = (E_0^y, E_1^y, \ldots, E_{N-1}^y)^T$, $E_z = (E_0^z, E_1^z, \ldots, E_{N-1}^z)^T$, $E_v = (C - zI)E_x - AE_z$, $E_w = (C - zI)E_y - BE_z$, $E_z = -G^{-1}(AE_v + BE_w)$, where the superscript T means the transposition of the matrix. z and E_4 are the eigenvalue and eigenvector of matrix Q, respectively. The introduction of two matrices E_v and E_w serves to derive the above eigenvalue equation (3). N stands for the number of beams participating in the diffraction. I_4 is a $4N \times 4N$ unit matrix. I is an $N \times N$ unit matrix. 0 is an $N \times N$ zero matrix. A, B and C are all $N \times N$ diagonal matrices. The diagonal elements of A, B and $C - zI$ are the X, Y and Z components of the wavevectors inside the crystal, respectively. The unknown z's are the eigenvalues of the matrix Q. $G = k^2(I + F)$, where F is an $N \times N$ matrix whose elements are given by $f_{mn} = \chi_{\mathbf{h}_m - \mathbf{h}_n} \cdot \chi_{\mathbf{h}_m - \mathbf{h}_n}$ is the electric susceptibility of the crystal for the $(\mathbf{h}_m - \mathbf{h}_n)$ reflection. G^{-1} is the inverse matrix of G. It should be noted that all the eigenvalues and eigenvectors of matrix Q are not real but complex.

The Cartesian coordinate frame (Fig. 1) adopted by Stetsko & Chang (1997) was chosen such that the z axis is perpendicular to the crystal entrance surface, pointing outward from the crystal, X and Y axes lie in the crystal entrance surface.

In this Cartesian coordinate frame, assuming that (X_m, Y_m, Z_m) are the coordinates of the reciprocal-lattice points involved in the diffraction lying on the surface of the Ewald sphere, and (X_c, Y_c, z) is the origin of the wavevectors of the waves propagating inside the crystal, where X_c and Y_c describe the position of the crystal-surface normal $\mathbf{n}$ on the surface (see Fig. 1). According to vector algebra, these diffracted waves can be expressed as

$$\mathbf{K}_{\mathbf{h}_m} = (X_m - X_c, Y_m - Y_c, Z_m - z) = (x_m, y_m, Z_m - z). \tag{6}$$

z is determined by the eigenvalue equation (3). There are $4N$ solutions of z. These solutions are the z components of the $4N$ origins of wavevectors, the so-called tie points of the

dispersion surface. Only those waves whose wavevectors are drawn from the tie points on the dispersion surface to the reciprocal-lattice points can survive inside the crystal.

The electric field associated with the wavevector $\mathbf{K}_{\mathbf{h}_m}$ is $\mathbf{E}_{\mathbf{h}_m} = (E_m^x, E_m^y, E_m^z)$.

In general, X_c and Y_c can be expressed in a spherical coordinate system as follows.

$$X_c = \frac{1}{\lambda}\cos(\theta)\cos(\phi), \quad Y_c = \frac{1}{\lambda}\cos(\theta)\sin(\phi), \tag{7a}$$

where $\theta = \theta_B + \Delta\theta$, $\phi = \phi_0 + \Delta\phi$.

The definition of θ and ϕ coordinates refers to Fig. 1. For convenience, ϕ_0 is usually chosen to be 0. That is, the incident beam lies in the xz plane. The quantity $\Delta\phi$ serves as the variable of the azimuthal scan around the z axis. The quantity $\Delta\theta$ stands for the angular deviation from the exact Bragg angle θ_B, serving as the variable for the rocking curve. For the normal incidence geometry (see Fig. 2), $[X_C, Y_C, Z_C = \sqrt{(1+\chi_0)/\lambda^2 - (X_C^2 + Y_C^2)}]$ is the center of the Ewald sphere. $(0, 0, 0)$ and (X_G, Y_G, Z_G) are the coordinates of the reciprocal-lattice point O for the incident reflection and point G for the back reflection. The corresponding diffracted wavevectors are $\mathbf{K}_O$ and $\mathbf{K}_G$, respectively. For normal-incidence geometry, when the values of X_c and Y_c are close to zero, consideration of the back diffraction in terms of the angular deviations, $\Delta\theta_X$ and $\Delta\theta_Y$, of the incident beam from the exact normal incidence is more convenient than the traditional spherical θ and ϕ. $\Delta\theta_X$ and $\Delta\theta_Y$ are also the angles of the crystal's rotation around the y and x axes, respectively. In this case, the coordinates X_c and Y_c of the crystal-surface normal $\mathbf{n}$ can be expressed as

$$X_c = \Delta\theta_X/\lambda, \; Y_c = \Delta\theta_Y/\lambda. \tag{7b}$$

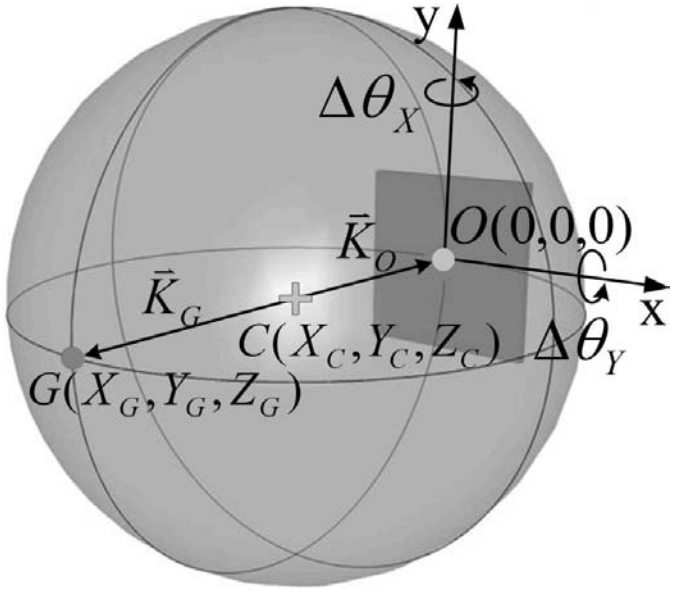

Figure 2
Schematic of the wavevectors for back diffraction in a two-beam case.

3. Boundary conditions for a single-crystal plate

The entries of eigenvectors E_4 are the x, y and z components of the electric fields inside the crystal. But the values of these entries are only the ratio between the wavefield amplitudes. Fortunately, according to boundary conditions, the electric fields outside the crystal could be determined. At the boundary between two different materials, the tangential components of the electric field $\mathbf{E}(r)$ and the magnetic field $\mathbf{H}(r)$ are continuous and the normal components of the electric displacement $\mathbf{D}(r)$ and the magnetic induction $\mathbf{B}(r)$ are also continuous. For a crystal plate, there are two boundaries, called the entrance and exit surface, respectively. Assuming that N waves are excited, each diffracted wave must obey the boundary conditions. This statement was formulated by Stetsko & Chang (1997) as follows.

$$\mathbf{E}_x: \quad \sum_{j=1}^{4N} c_j E_m^x(j)\psi_{jl} = E_{(e)}^x \delta_{m0}^{l1} + E_{ml}^x \varphi_{ml} \tag{8}$$

$$\mathbf{E}_y: \quad \sum_{j=1}^{4N} c_j E_m^y(j)\psi_{jl} = E_{(e)}^y \delta_{m0}^{l1} + E_{ml}^y \varphi_{ml} \tag{9}$$

$$\mathbf{D}_z: \quad \sum_{j=1}^{4N} c_j \Big[E_m^z(j) + \sum_{n=0}^{N-1} \chi_{h_m - h_n} E_n^z(j)\Big]\psi_{jl} = E_{(e)}^z \delta_{m0}^{l1} + E_{ml}^z \varphi_{ml} \tag{10}$$

$$\mathbf{H}_x: \quad \sum_{j=1}^{4N} c_j [z_{mj} E_m^y(j) - y_m E_m^z(j)]\psi_{jl} = (K_m^z E_{(e)}^y - y_m E_{(e)}^z)\delta_{m0}^{l1} + [(-1)^l K_m^z E_{ml}^y - y_m E_{ml}^z]\varphi_{ml} \tag{11}$$

$$\mathbf{H}_y: \quad \sum_{j=1}^{4N} c_j [x_m E_m^z(j) - z_{mj} E_m^x(j)]\psi_{jl} = (x_m E_{(e)}^z - K_m^z E_{(e)}^x)\delta_{m0}^{l1} + [x_m E_{ml}^z - (-1)^l K_m^z E_{ml}^x]\varphi_{ml} \tag{12}$$

$$\mathbf{B}_z: \quad \sum_{j=1}^{4N} c_j [y_m E_m^x(j) - x_m E_m^y(j)]\psi_{jl} = (y_m E_{(e)}^x - x_m E_{(e)}^y)\delta_{m0}^{l1} + [y_m E_{ml}^x - x_m E_{ml}^y]\varphi_{ml}, \tag{13}$$

which involve the relations $\mathbf{D}_{\mathbf{h}_m} = \varepsilon_0(\mathbf{E}_{\mathbf{h}_m} + \sum_{n=0}^{N-1} \chi_{\mathbf{h}_m - \mathbf{h}_n} \mathbf{E}_{\mathbf{h}_n})$ and $\mathbf{B} = \mu\mathbf{H}$, $\mathbf{H}_{\mathbf{h}_m} = (\mathbf{K}_{\mathbf{h}_m} \times \mathbf{E}_{\mathbf{h}_m})/k$ for non-magnetic materials, *i.e.* $\mu = 1$. Because the number of eigenvectors of the matrix Q is $4N$, the summation must be taken over $j = 1, \ldots, 4N$. The Kronecker delta is defined as $\delta_{m0}^{l1} = 1$ if $m = 0$ and $l = 1$; otherwise, $\delta_{m0}^{l1} = 0$. $l = 1$ means the entrance surface and $l = 2$ stands for the exit surface. $E_{(e)}^x$, $E_{(e)}^y$ and $E_{(z)}^z$ are the x, y and z components of the electric field of the incident beam. E_{ml}^x, E_{ml}^y and E_{ml}^z are the x, y and z components of the electric fields of the diffracted waves in front of ($l = 1$) and behind ($l = 2$) the plane-parallel crystal. The subscript m takes the values $m = 0, \ldots, N-1$. z_{mj}, defined as $z_{mj} = Z_m - z_j$, are the z components of the wavevectors of the diffracted waves inside the crystal. K_m^z and $-K_m^z$ are the z components of the wavevectors of the outgoing diffracted waves at the exit and entrance side of the crystal plate, respectively. K_m^z is defined as $K_m^z = -[k^2 - (x_m^2 + y_m^2)]^{1/2}$. $\psi_{j1} = \varphi_{m1} = 1$, $\psi_{j2} = \exp(2\pi i z_{mj} t)$

and $\varphi_{m2} = \exp(2\pi i K_m^z t)$, where t is the thickness of the crystal plate.

Merging the above equations (8)–(13) by a linear combination and eliminating the electric fields E_{ml}^x, E_{ml}^y and E_{ml}^z outside the crystal, the new equations take the following forms, where only the unknown c_j are left. The detailed deviation can be found in the papers by Stetsko & Chang (1997) and Chang (2004).

$$\sum_{j=1}^{4N} c_j \left\{ [z_{mj} + (-1)^{l-1} K_m^z] E_m^x(j) + x_m \sum_{n=0}^{N-1} \chi_{h_m - h_n} E_n^z(j) \right\} \psi_{jl} = 2K_m^z E_{(e)}^x \delta_{m0}^{l1} \quad (14)$$

$$\sum_{j=1}^{4N} c_j \left\{ [z_{mj} + (-1)^{l-1} K_m^z] E_m^y(j) + y_m \sum_{n=0}^{N-1} \chi_{h_m - h_n} E_n^z(j) \right\} \psi_{jl} = 2K_m^z E_{(e)}^y \delta_{m0}^{l1}. \quad (15)$$

After expanding the above equations (14)–(15) over $j = 1, \ldots, 4N$, $m = 0, \ldots, N-1$, and $l = 1, 2$, these equations can be combined and presented in a linear system, like $A'X = B'$. Here, A' is a $4N \times 4N$ square matrix. X and B' are $4N \times 1$ column matrices. The entries of column matrix X are the unknown c_j. The entries of column matrix B' are related to the polarization of the electric field and wavevector of the incident beam. The unknown c_j can be obtained by calling standard subroutines, in particular, the subroutines of the IMSL library (Compaq Visual Fortran 6.6b, 2002) of Visual Fortran. Once the values of the unknown c_j are determined, the next step is to substitute the constants c_j back into the original boundary conditions, (8)–(10). Eventually, the electric fields E_{ml}^x, E_{ml}^y and E_{ml}^z of the diffracted waves outside the crystal can be obtained.

4. Diffraction in an X-ray Fabry–Perot cavity

In an optical Fabry–Perot cavity, the total reflection and transmission amplitudes of the cavity can be expressed in a closed form by summing the multiply reflected amplitudes from two mirrors. Similarly, the total amplitudes can be obtained by the same token for an X-ray Fabry–Perot cavity by considering the multiply diffracted waves between the two crystal plates. In fact, the reflectivity and transmission had been derived from the dynamical theory by Caticha *et al.* (1996), Kikuta *et al.* (1998), Kohn *et al.* (2000), Shvyd'ko (2004) and many others.

According to Kohn *et al.* (2000), the dynamical theory of two-beam back diffraction at normal-incidence geometry gives the expressions for the transmission and reflection amplitudes of X-rays from a single plate. The results are then generalized for back diffraction from a two-layer system by further deducing the recursion relations for transmission and reflection amplitudes for a multilayer crystalline system. Each layer is viewed as a crystal plate. The recursion relations are

$$t_m^{(k)} = \frac{t_k t_m^{(k-1)}}{1 - r_k \bar{r}_m^{(k-1)}}, \quad r_m^{(k)} = r_m^{(k-1)} + \frac{t_m^{(k-1)} \bar{t}_m^{(k-1)} r_k}{1 - r_k \bar{r}_m^{(k-1)}}, \quad (16)$$

where $r_m^{(k)}$ and $t_m^{(k)}$ are the reflection and transmission amplitudes of a k-layer system; $r_m^{(k-1)}$ and $t_m^{(k-1)}$ are the reflection and transmission amplitudes of the $k-1$ layer system. r_k and t_k are the reflection and transmission amplitudes of the individual kth layer. If a gap exists between two successive layers filled with a non-diffracting medium, its susceptibility is equal to zero.

Now consider a system consisting of only three layers, in which the first and third layers are crystal plates parallel to each other; the middle layer is filled with a non-diffracting medium. This system can be used to represent a two-plate X-ray Fabry–Perot resonator. Assume that the thicknesses of the first and second plates are d_1 and d_2, respectively, and the middle layer is actually a gap of size d_g. The transmission and reflection amplitudes for each layer are described as follows (Kohn *et al.*, 2000). At the first layer: $t_1 = t(d_1)$, $\bar{t}_1 = \bar{t}(d_1)$, $r_1 = r(d_1)$, $\bar{r}_1 = \bar{r}(d_1)$; at the middle layer: $r_2 = \bar{r}_2 = 0$, $t_2 = \exp[(ikd_g/2\gamma_0)\chi_g]$, $\bar{t}_2 = \exp[(ikd_g/2\gamma_0)(\chi_g - \alpha)]$; and at the third layer: $r_3 = r(d_2)\exp(ihu)$, $\bar{r}_3 = \bar{r}(d_2)\exp(-ihu)$, $t_3 = t(d_2)$, $\bar{t}_3 = \bar{t}(d_2)$. h is the modulus of the reciprocal-lattice vector of (12 4 0) and $u = d_g$.

Inserting these expressions into the recursion relations (16), the reflection and transmission amplitudes of an X-ray Fabry–Perot cavity are derived as

$$r_m = r(d_1) + \frac{t(d_1)\bar{t}(d_1) r(d_2) \exp(i\phi)}{1 - \bar{r}(d_1) r(d_2) \exp(i\phi)} \quad (17)$$

$$t_m = \frac{t(d_1) t(d_2) \exp(i\phi_g)}{1 - \bar{r}(d_1) r(d_2) \exp(i\phi)}, \quad (18)$$

where $\phi = hd_g + 2\phi_g - (kd_g/2\gamma_0)\alpha$, $\phi_g = (kd_g/2\gamma_0)\chi_g$ and $k = 1/\lambda$. α is the angular deviation from the Bragg condition, γ_0 is the direction cosine of the incident beam with respect to the inward surface normal. d_g is the width of the gap between the two crystal plates, d_1 and d_2 are the thicknesses of the first and second crystal plates, respectively. χ_g is the electric susceptibility of the gap material. $r(d_1)$ and $t(d_1)$ are the reflection and transmission amplitudes of the first plate in the direction of the incident beam and $t(d_2)$ is for the second plate. $\bar{r}(d_1)$ and $\bar{t}(d_1)$ are the reflection and transmission amplitudes of the first plate in the direction of the back diffraction. These reflection and transmission amplitudes $\bar{r}(d_1)$, $\bar{t}(d_1)$, $r(d_1)$ and $t(d_1)$ are given by the numerical solutions of the dynamical theory. Similar derivations are also reported by Caticha *et al.* (1996) and Shvyd'ko (2004). The total reflection and transmission amplitudes expressed as a geometrical series implies that the coherent length of the incident beam was assumed to be infinite so that an infinite number of forward transmissions and back reflections occur inside the cavity.

5. Conditions for dynamical calculations

The lattice parameter of 5.4309 Å of silicon is used throughout the calculations The polarization of the electric field of the incident beam is chosen along the [100] direction in the Cartesian coordinate frame. The values of polarization factors are put into the right-hand side of equations (14) and (15). The thickness of each silicon crystal plate is 70 µm (= $d_1 = d_2$) with a 100 µm (= d_g) gap between the two plates (see Fig. 3). The

energy of the incident beam is chosen as 14.4388 keV. The atomic scattering factors of Si are used according to *International Tables for Crystallography* (2004). The anomalous corrections of atomic scattering factors are obtained from the NIST website (http://physics.nist.gov/PhysRefData/FFast/Text/cover.html). The distribution of the 24 reciprocal-lattice points (r.l.p.) over the surface of the Ewald sphere is shown in Fig. 4. If the Ewald sphere is viewed along the Y axis, 24 r.l.p.'s lie in three different planes. The first plane, $h = 6$, consists of (682), (68$\bar{2}$), (646), (64$\bar{6}$), (606), (60$\bar{6}$), (6$\bar{4}$2) and (6$\bar{4}\bar{2}$). The second, $k = 2$, is composed of (426), (42$\bar{6}$), (826), (82$\bar{6}$), (1222), (122$\bar{2}$), (022) and (02$\bar{2}$). The third, $l = 0$, consists of (000), (1240), (880), (1200), (8$\bar{4}$0), (480), (4$\bar{4}$0) and (040). All of them can be classified into three kinds of diffraction geometry. The (8$\bar{4}$0) and (480) reflected waves, called Bragg-surface waves, whose Bragg angles are 45°, propagate along the crystal surface. The other 22 beams can be divided into two categories: Bragg reflection type and Laue transmission type. If all of the 24 r.l.p.'s on the surface of the Ewald sphere are first projected onto the xy plane, then 22 lines connecting these projected points to the origin are drawn, and (1240) and (000) are projected to (0,0). Only nine radial lines are visible due to overlapping of the lines (See Fig. 5).

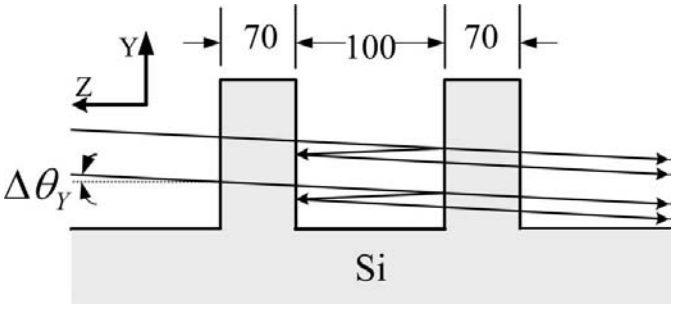

Figure 3
Schematic of an X-ray Fabry–Perot cavity with $d_1 = d_2 = 70$ μm and $d_g = 100$ μm.

6. Results

6.1. Intensity distributions

Fig. 6(*a*) represents the calculated intensity map of the reflected (1240) beam as a function of $(\Delta\theta_X, \Delta E)$ in the two-beam diffraction, *i.e.* (000)(1240) with $\Delta E = E - 14.4388$ keV for a two-plate crystal. It should be noted that the photon energy in vacuum for the exact back diffraction of (1240) is $E_0 = 14438.8$ eV, calculated from $2d_{1240} = \lambda = hc/E_0$ (in vacuum). The radius of the Ewald sphere seen by the crystal is n/λ. The effective energy corresponding to this Ewald sphere is nE_0, where n is the index of refraction. Hence the energy difference ΔE of X-rays in the silicon crystal and in vacuum is $(1 - n)E_0$. Here, we refer to ΔE as the energy difference in the crystal, which is also adopted in the experiment. When the energy deviation ΔE was chosen as 12 meV, indicated by the gray line, there are five fringes within an angular range of ±0.1° (Fig. 6*b*). This energy was used to calculate the angular intensity distributions of the reflected (1240) and transmitted (000) diffracted beams as a function of $(\Delta\theta_X, \Delta\theta_Y)$ in the 24-beam case for a two-plate cavity (see Figs. 7*a* and 7*b*). If ΔE is varied, the number of fringes or the interference pattern will also change. This fact can be used for energy calibration.

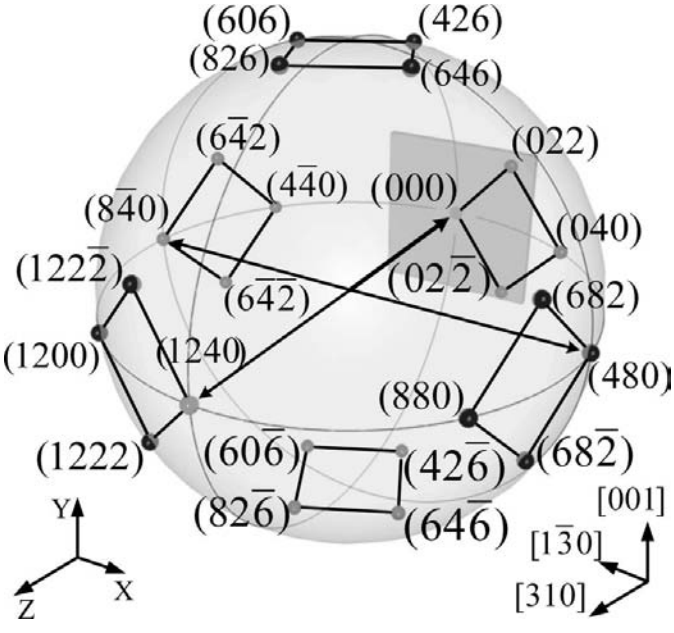

Figure 4
The distribution of the reciprocal-lattice points on the surface of the Ewald sphere for the 24-beam case. The wavevectors of the (000), (1240), (8$\bar{4}$0) and (480) are shown. Otherwise they are depicted as polyhedra.

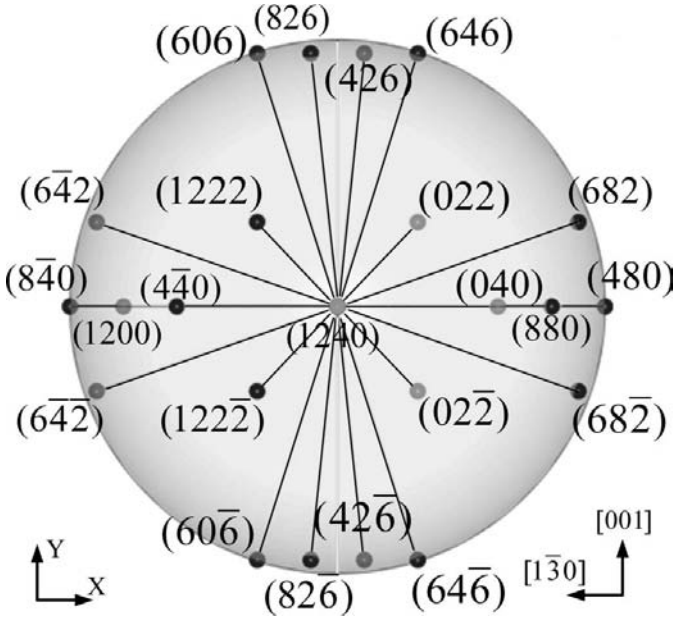

Figure 5
The distribution of the 24 r.l.p.'s projected onto the xy plane shows nine radial lines.

Fig. 7 shows the calculated intensity distributions of the reflected beam (1240) (Fig. 7*a*) and the transmitted beam (000) (Fig. 7*b*) as a function of $(\Delta\theta_X, \Delta\theta_Y)$ in the 24-beam case for a two-plate crystal at $\Delta E = 12$ meV off the exact resonance energy. Five concentric rings exist within angular ranges $\pm 0.1^\circ$ due to the interference of the multiply forward and backward reflected coherent X-rays from the two plates. Nine radial lines ($L1$–$L9$) of diffraction are generated by the multiple-beam interactions. They correspond to nine coplanar diffractions, belonging to nine zone axes, respectively. The involved multiple beams for each line are respectively as follows. $L1$: (1200), (040), (880), (4$\bar{4}$0), (480), (8$\bar{4}$0); $L2$: (122$\bar{2}$) (022); $L3$: (60$\bar{6}$), (646); $L4$: (82$\bar{6}$), (426); $L5$: (826), (42$\bar{6}$); $L6$: (606), (64$\bar{6}$); $L7$: (1222), (02$\bar{2}$); $L8$: (68$\bar{2}$), (64$\bar{2}$); $L9$: (682), (6$\bar{4}$2). Only $L1$ is an eight-beam diffraction, the others are four-beam diffractions. The directions of the nine radial lines of diffraction shown in Fig. 7(*a*) are perpendicular to those of the radial lines connecting the reciprocal-lattice points shown in Fig. 5. This is because the wavevector is perpendicular to the electric field for the transverse X-ray waves. The calculated results agree with the experimental data (see Fig. 7*c*).

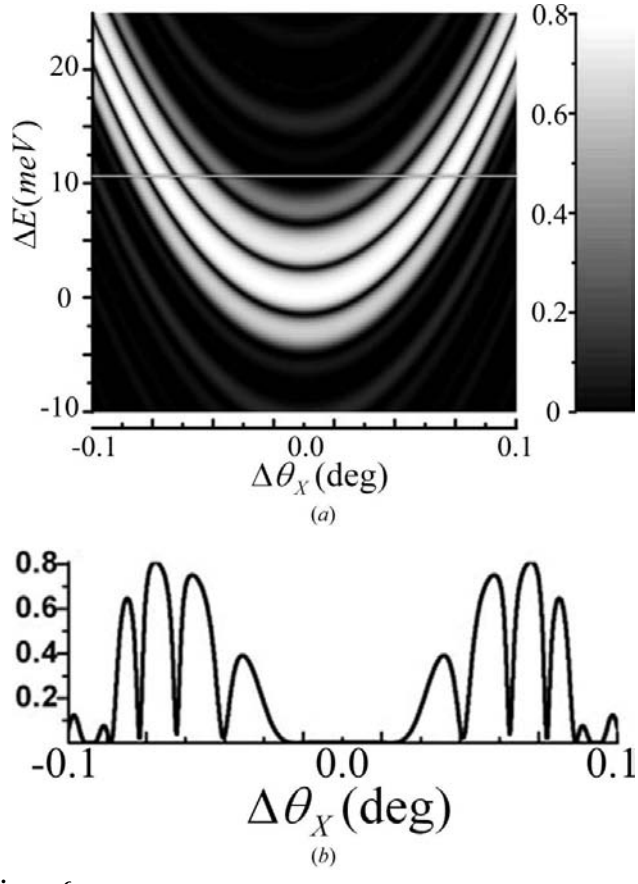

Figure 6
(*a*) The calculated intensity distributions of the reflected (1240) wave as a function of $(\Delta\theta_X, \Delta E)$ in the two-beam case, *i.e.* (1240) and (000), for a two-plate crystal at $\Delta\theta_Y = 0$. (*b*) The section of (*a*) at $\Delta E = 12$ meV, indicated by the horizontal gray line, shows five fringes within the angular range $\pm 0.1^\circ$.

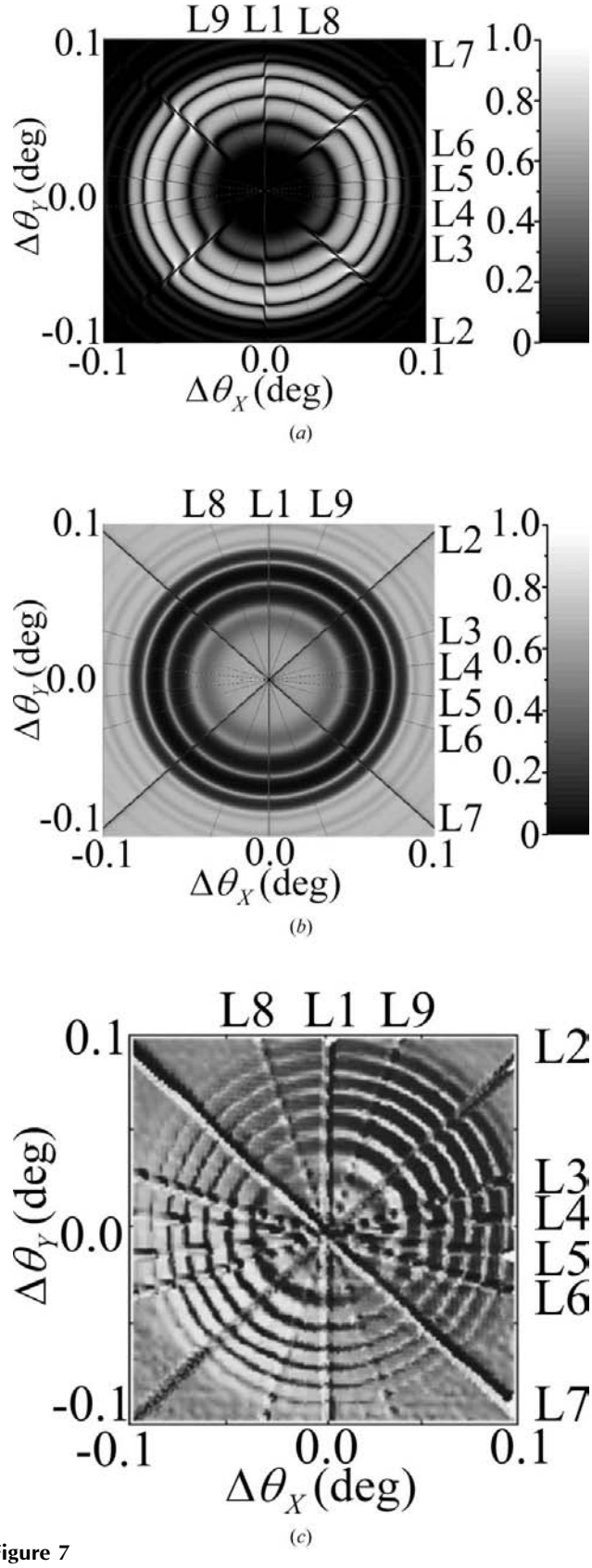

Figure 7
Calculated interference pattern of (*a*) the reflected (1240) and (*b*) the transmitted (000) beams in the 24-beam case for a two-plate crystal at $\Delta E = 12$ meV. (*c*) Experimentally measured interference pattern of the transmitted (000) beam for a two-plate crystal at $\Delta E = 12$ meV (Chang *et al.*, 2005, 2006). Five concentric rings are within the angular range $\pm 0.1^\circ$.

6.2. Dispersion surface

The dispersion surface contains 96 sheets for the 24-beam case, *i.e.* $4 \times 24 = 96$, which result from the intersection of 24 spheres centered at the 24 reciprocal-lattice points, with the radii n/λ, where n is the index of refraction. The crystal-surface normal **n** intersects each sphere twice. Since there are two polarizations, σ and π, the number of dispersion sheets is then doubled, that is $4N = 2 \times 2N$. Taking the two-beam symmetric Bragg diffraction as an example to illustrate the origin of 4N dispersion sheets, in Fig. 8 the normal **n** intersects the dispersion surface (solid curves that are rather close to spheres O and G of the radii n/λ) at the tie points z_1, z_2, ... and z_8. Their positions are determined from the real parts of the eigenvalues of matrix Q for the (1240) two-beam diffraction. According to Ewald & Héno (1968), only the diffracted waves with wavevector origins z_3, z_4, z_5 and z_6, which are close to the Laue point (point of intersection of spheres O and G of the radii n/λ), dominate in diffraction. The spheres O and G of the radii $1/\lambda$ that represent the loci of the origins of the wavevectors of diffracted waves propagating in vacuum (outside the crystal) are shown in the xz plane of Fig. 8 as dashed circles. The relative difference in the lengths of wavevectors between the diffracted waves propagating outside and inside the crystal is only about $1 - n = 1 - \sqrt{1 + \chi_0} \approx |\chi_0|/2 \sim 10^{-5}$–$10^{-6}$. By translating the normal **n** along the crystal surface, the whole dispersion surface can be mapped out. That is, solving the eigenvalues of matrix Q for varying (X_c, Y_c). If we cut the dispersion surface by the xy plane in the vicinity of the middle point between the two reciprocal-lattice points O and G, then the dispersion curves look like the calculated curves shown in Fig. 9(b), which are symmetric about $\Delta\theta_X = 0^\circ$. The regions for $\Delta\theta_X = 0.06$–0.08° and $\Delta\theta_X = -0.06$–-0.08° are the ranges of total reflection. These features are characteristic of a two-beam back diffraction (Authier, 2001).

If 24 beams are excited inside the crystal, there are 24 spheres intersecting with each other in the reciprocal space. It is too complicated to draw all of the dispersion sheets. Here, we consider only the dominant modes (formally enumerated as 47–50) for reflections (000) and (1240), and show their dispersion sheets on appropriate sections of the dispersion surface. However, the dispersion sheet of a given mode usually crosses that of other modes when Bragg-type reflection is involved. This cross-over makes the identification of modes difficult. To overcome this difficulty, we first enumerate the eigenvalues in an order according to the values of their imaginary parts, and then consider the values of their corresponding real parts. Usually the signs of the imaginary parts of eigenvalues for the same mode at adjacent angular settings are the same. The variation on the value of the imaginary part of the eigenvalue for the same mode at the next closest angular

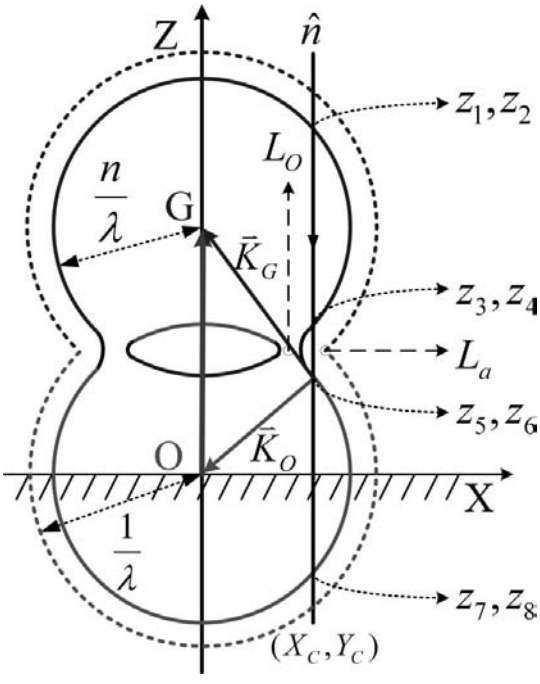

Figure 8
Schematic section of the dispersion surface of two-beam (1240) diffraction in reflection geometry (L_a: Laue point. L_o: Lorentz point).

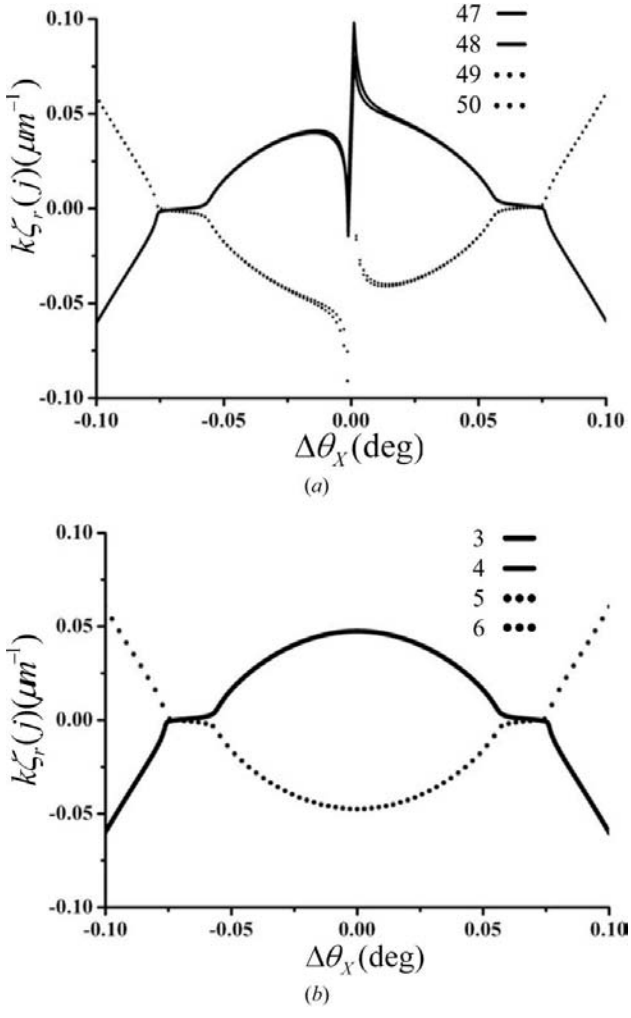

Figure 9
Calculated sections of (a) the dispersion surface of the 24-beam diffraction for modes 47–50 at $\Delta\theta_Y = 0$ and (b) the dispersion surface of the two-beam diffraction (000)(1240) for modes 3–6 at $\theta_Y = 0$.

setting should be very small. Once the mode is identified according to its imaginary part of the eigenvalue, the corresponding real part, *i.e.* the coordinates of the tie point, is determined. If the locus of the real part of the tie point shows singularity at an angular setting, then we need to re-examine both the real and imaginary parts of the eigenvalues in the vicinity of that angular setting so that a reasonably continuous curve is obtained. Based on these criteria, the section of dispersion surface and linear absorption coefficient are sketched as shown in Figs. 9(*a*) and 10, respectively.

As can be seen in Fig. 9(*a*), modes 47 and 48 are respectively associated with the σ and π polarized (000) reflection, while modes 49 and 50 are respectively associated with the σ and π polarized (12 4 0) reflection. The angular regions for $\Delta\theta_X$ = 0.06–0.08° are the range of total reflection. Originally, there were 701 data points calculated within the angular region $\pm0.1^\circ$, but seven undetermined points are neglected at $\Delta\theta_X$ = 0.0. This leads to the sharp curves at $\Delta\theta_X = 0.0$.

For the two-beam case, modes 3 and 4, shown in Fig. 9(*b*), are *O*-like, *i.e.* *O* = (000), while modes 5 and 6 are *G*-like with *G* = (12 4 0). The dispersion curves of modes 3 and 4 are overlapping, and so are modes 5 and 6. In contrast, the dispersion sheets in the 24-beam diffraction are distorted near the exact 24-beam diffraction position ($\Delta\theta_X = 0$) due to multiple-beam interaction.

6.3. Linear absorption coefficients

The linear absorption coefficients are equal to $2\pi\,\mathrm{Im}(z_j)$, where z_j are the eigenvalues of matrix Q. Fig. 10 shows the calculated linear absorption coefficients of the 24-beam case for modes 47–50 at $\Delta\theta_Y = 0$. There are four dominant modes, labeled as 47–50, among which only the two with positive absorption, modes 47 and 48, can survive inside the crystal plate. The reason is the following: a phase factor $\psi_{j2} = \exp(2\pi i z_{mj} t)$ appears in the boundary conditions (8)–(13) at the exit surface, where $z_{mj} = Z_m - z_j$. The eigenvalues z_j are complex, which can be explicitly expressed as the sum of the real and imaginary parts. Hence, ψ_{j2} can be expressed as $\exp[2\pi\,\mathrm{Im}(z_j)t]\exp\{2\pi i[(Z_m - \mathrm{Re}(z_j)]t\}$. Looking at this expression, only modes 47 and 48 with $\mathrm{Im}(z_j) < 0$ are allowed for the sake of conservation of energy. The absorption curves of modes 47 and 48 coincide with each other for most of the angular settings except for the region near the exact 24-beam diffraction position. This implies that some energy is transferred to multiple diffraction channels, leading to a decrease in the linear absorption coefficient near the exact 24-beam position. For modes 49 and 50, their amplitudes at the exit surface are greater than those at the entrance surface due to $\mathrm{Im}(z_j) > 0$. These modes are associated with the diffraction from the back surface of the crystal. For a sufficiently thick crystal, these modes can be neglected. The fact that the linear absorption coefficients of modes 47 and 48 have significant values in the angular regions $\Delta\theta_X = \pm0.06 - \pm0.08^\circ$ (the ranges of total reflection) indicates that standing waves are formed inside the crystal and the incident energy is efficiently absorbed by the crystal. Originally, there were 701 data points calculated within the angular region, but 7 undetermined points are neglected at $\Delta\theta_X = 0.0$.

6.4. Excitation of mode

The excitation of mode is defined as

$$\mathrm{Ex}(j) = \frac{|S(j)\tilde{\boldsymbol{n}}|}{|S_O\tilde{\boldsymbol{n}}|} = \frac{\sum_m \gamma_m(j)[|E_m(j)|^2]}{\gamma_O|E_O|^2},$$

where $\tilde{\boldsymbol{n}}$ is the unit vector of the crystal normal, $\gamma_m(j)$ is the direction cosine of the mth diffracted wave of the jth mode with respect to the inward surface normal $\tilde{\boldsymbol{n}}$. γ_O is the direction cosine of the incident beam, $S(j)$ is the Poynting vector of the jth mode and S_O is the Poynting vector of the incident beam. Since the direction of energy propagation is nearly normal to the dispersion surface, the excitation of mode indicates the

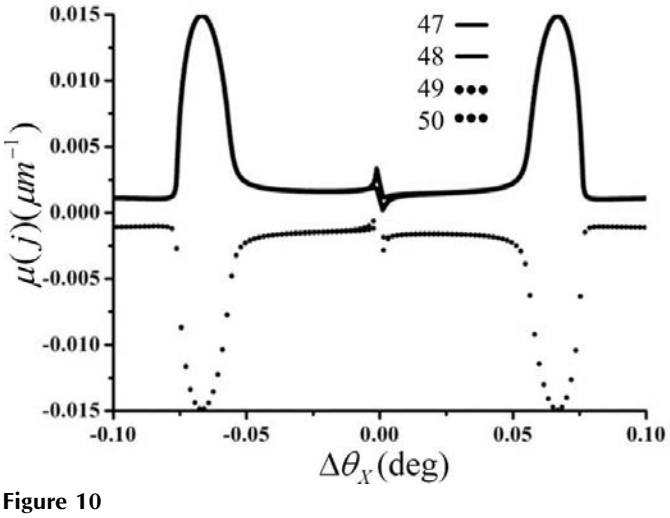

Figure 10
Calculated linear absorption coefficients of the 24-beam diffraction for modes 47–50 at $\Delta\theta_Y = 0$.

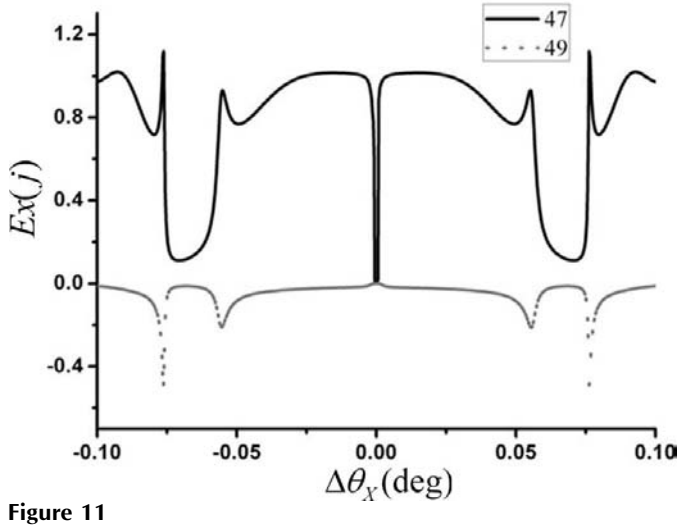

Figure 11
Excitations of mode of the 24-beam diffraction for mode 47 and 49 at $\theta_Y = 0$.

energy flow of the traveling electromagnetic wave. If it is a standing wave, the Poynting vector is zero.

Fig. 11 shows the excitations of mode of the 24-beam case for modes 47 and 49 at $\Delta\theta_Y = 0$. The drop of the excitation angular regions $\Delta\theta_X = \pm 0.06 - \pm 0.08^\circ$ is again due to the total reflection because most of the incident energy is reflected, while near the exact 24-beam region the drop is due to the multiple diffraction which takes away the energy. The negative excitation is associated with the (1240) back-reflected wave, where the direction cosine is negative. The undulations of the excitation outside the central (total reflection) region are due to the crystal thickness effects, the *Pendellosung* (Authier, 2001).

6.5. Phase of the transmitted *O* wave

Fig. 12 depicts the phase of the transmitted (000) wave *versus* $\Delta\theta_X$, the angular deviation from the exact 24-beam diffraction position for mode 47. Far from the total reflection region ($\Delta\theta_X = 0.06$–0.08°), the transmitted *O* wave is in phase with that of the incident wave. The phase in the total reflection range, not including the 24-beam position, varies first from 0 to -175° and then stays at -175°. In the vicinity of the 24-beam position (about 0.0023°), the phase is drastically changed from -175 to 0 and then 0 to -175°. This phase change is mainly due to the exact phase matching of the transmitted wave with the incident wave at the exact 24-beam diffraction position. For a non-absorbing crystal, the variation in phase can be as large as 180°.

7. Conclusions

We have carried out dynamical calculations for the back diffraction of (1240) in a monolithic two-plate silicon cavity at a photon energy of 14.4388 keV, at which the 24-beam diffraction takes place. The section of the dispersion surface, linear absorption coefficients, wavefield intensities and excitation of mode are calculated. The calculated intensity distribution of the transmitted beam is in good agreement with the observed one. The developed Fortran program for solving the fundamental equation of wavefield based on the dynamical theory of X-ray diffraction is also briefly outlined.

From the viewpoint of X-ray optics, the effect of multiple Bragg diffraction on an X-ray Fabry–Perot resonator seems to reduce the reflectivity for the back-diffraction channel and the finesse of the resonator decreases because part of the incident energy is taken away by multiple diffractions. However, the involvement of high-energy photons in the experiments makes it easier to have suitable high-energy resolution monochromators available for cavity experiments. If lower-energy photons are used, then it would be difficult to reach the required energy resolution, *i.e.* $\Delta E/E \approx 10^{-8}$ for monochromators. Consequently, interference due to cavity resonance would be very hard to detect because of the poor longitudinal coherence (Chang *et al.*, 2006). Moreover, under the cavity resonance condition, X-ray standing waves of a period of $\lambda/2$ are expected to be formed in between the two crystal plates. The dynamical calculation indeed shows this standing-wave feature (not shown here). The details will be reported elsewhere. The current 24-beam dynamical calculations offer us more information about the X-ray diffraction processes in this type of X-ray resonator, although the fine structure and asymmetry of profiles of resonance fringes at the intersection with the radial diffraction lines were not observed in the experiments due to limited resolution resulting from crystal imperfection, temperature, surface roughness and lattice distortion.

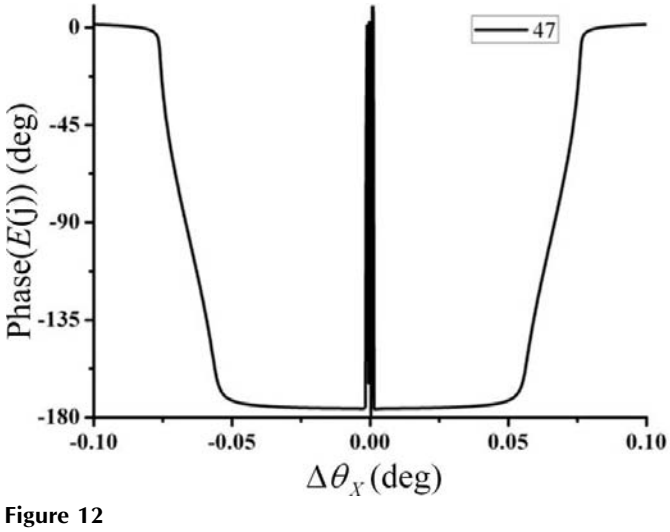

Figure 12
Phase of the transmitted (000) wave *versus* $\Delta\theta_X$ of the 24-beam diffraction for mode 47 at $\Delta\theta_Y = 0$.

APPENDIX *A*
Procedure for the programming for dynamical calculation

The procedures for developing an algorithm for multibeam diffraction involving a back reflection in two crystal plates are briefly outlined below.

A1. A single-crystal plate

1. Set up a Cartesian coordinate frame for the diffraction geometry at the entrance surface of the crystal plate.

2. Input the lattice constants of the crystal, the wavelength of the incident beam, the back reflection (the so-called primary reflection) and all the reciprocal-lattice points involved in a multiple diffraction, and calculate the coordinates (X_m, Y_m, Z_m) of the reciprocal-lattice points when situated on the surface of the Ewald sphere.

3. Input all atoms' fractional positions within a unit cell and their atomic scattering factors, calculate the electric susceptibility $\chi_{\mathbf{h}_m - \mathbf{h}_n}$ of reflections $\mathbf{h}_m - \mathbf{h}_n$ and construct the G and G^{-1} matrices. G^{-1} can be obtained by calling the subroutine DLINCG (N, G, N, IG, N) of the IMSL library. G^{-1}, the inverse of G, will be stored in the *IG* matrix after calling the subroutine. N is the rank of the matrix G.

4. Choose the origin (X_C, Y_C) for the wavevectors $\mathbf{K}_{\mathbf{h}_m}$ and calculate the matrix elements of matrices A, B and C.

5. Put A, B, C, G and G^{-1}, obtained from steps 3–4, into the matrix Q.

6. Call the subroutine DEVCCG (4N, Q, 4N, EVAL, EVEC, 4N) of the IMSL library to calculate the eigenvectors and eigenvalues of matrix Q. The 4N solved eigenvalues will be stored in the EVAL column matrix. Eigenvectors will be stored in the EVEC matrix. The EVEC matrix consists of $4N$ column matrices. Each column matrix is a matrix E_4 [see equation (5)].

7. Extract the electric fields $E_m^x(j)$, $E_m^y(j)$ and $E_m^z(j)$, respectively, from the matrix EVEC. Note that $E_m^z = -G^{-1}(AE_m^v + BE_m^w)$, $m = 0, 1, \ldots, N-1, j = 1, \ldots, 4N$.

8. Calculate the z components of the wavevectors for the diffracted waves outside and inside the crystal, *i.e.* $K_m^z = -[k^2 - (x_m^2 + y_m^2)]^{1/2}$ and $z_{mj} = Z_m - z_j$, respectively.

9. Construct a linear system $A'X = B'$ according to equations (14)–(15), and calculate the matrix elements for A' and B'.

10. Call the subroutine DLSLCG (4N, A′, 4N, B′, 1, X) of the IMSL library to solve the linear system $A'X = B'$. The output c_j are stored in the column matrix X.

11. Substitute the constant c_j into equations (8)–(10) and calculate the electric field of the diffracted waves outside the crystal.

12. Choose another origin (X_C, Y_C) and repeat steps 4–12 to calculate the reflectivity and construct the two-dimensional intensity distribution map. Here, two 'do loops' are required to vary X_C and Y_C, respectively.

A2. A two-plate crystal cavity

1. In general, the angular deviation α is given by (Shvyd'ko *et al.*, 1998, 2004)

$$\alpha = 4(E_B/E)[(E_B/E) - \sin\theta].$$

The program adopts this expression to calculate the reflectivity and transmissivity.

2. The reflection and transmission amplitudes of the individual crystal plate are derived at step 11 of §$A1$. Putting them into equations (17)–(18), one obtains the total reflection and transmission amplitudes of an X-ray Fabry–Perot cavity. Note that in §$A1$, step 11, if the amplitude of the electric field of the incident beam is assumed to be unity, the amplitude of the electric field of the diffracted beam outside the crystal is equal to the reflection amplitude.

Note:

1. Consider the equations involving the exponential function $\psi_{j2} = \exp(2\pi i z_{mj} t)$. If the exponent $2\pi\,\mathrm{Im}(z_{mj})t$ is greater than 709.8, then it leads to overflow on the exponential function because the maximum floating-point number stored in a computer is about 1.65×10^{308}. Refer to Stetsko & Chang (1997) to solve this problem.

2. Every time the subroutine is called to solve the eigenvalue equation, the order of eigenvalues and the associated eigenvectors are random. Only by rearranging the eigenvalues and eigenvectors by hand using graphical software will the section of the dispersion surface, the absorption coefficient and mode excitation with respect to modes of propagation be correctly assigned. This task is usually very time consuming.

3. Compaq Visual Fortran 6.6b (2002) contains the IMSL library.

References

Authier, A. (2001). *Dynamical Theory of X-ray Diffraction*, ch. 5, pp. 148–154. Oxford University Press.

Bond, W. L., Duguay, M. A. & Rentzepis, P. M. (1967). *Appl. Phys. Lett.* **10**, 216–218.

Caticha, A., Aliberty, K. & Caticha-Ellis, S. (1996). *Rev. Sci. Instrum.* **67**, 3380.

Caticha, A. & Caticha-Ellis, S. (1982). *Phys. Rev. B*, **25**, 971–983.

Caticha, A. & Caticha-Ellis, S. (1990). *Phys. Status Solidi A*, **119**, 643–654.

Chang, S.-L. (2004). *X-ray Multiple-Wave Diffraction: Theory and Application*, ch. 7. Berlin: Springer-Verlag.

Chang, S.-L., Stesko, Y. P., Tang, M.-T., Lee, Y.-R., Sun, W.-H., Yabashi, M. & Ishikawa, T. (2005). *Phys. Rev. Lett.* **94**, 174801.

Chang, S.-L., Stesko, Y. P., Tang, M.-T., Lee, Y.-R., Sun, W.-H., Yabashi, M., Ishikawa, T., Wu, H.-H., Shew, B.-Y., Lin, Y.-H., Kuo, T.-T., Tamssaku, K., Miwa, D., Chen, S.-Y., Chang, Y.-Y. & Shy, J.-T. (2006). *Phys. Rev. B*, **74**, 134111.

Colella, R. & Luccio, A. (1984). *Opt. Commun.* **50**, 41–44.

Compaq Visual Fortran 6.6b (2002). Professional Edition including the IMSL library.

Darwin, C. G. (1914). *Philos. Mag.* **27**, 675–690.

Deslattes, R. D. (1968). *Appl. Phys. Lett.* **12**, 133–135.

Ewald, P. P. (1916). *Ann. Phys.* **49**, 1–38.

Ewald, P. P. & Héno, Y. (1968). *Acta Cryst.* A**24**, 5–15.

International Tables for Crystallography (2004). Vol. C, 3rd ed. Dordrecht: Kluwer Academic Publishers.

Kikuta, S., Imai, Y., Iizuka, T., Yoda, Y., Zhang, X.-W. & Hirano, K. (1998). *J. Synchrotron Rad.* **5**, 670–672.

Kohn, V. G., Shvyd'ko, Yu. V. & Gerdau, E. (2000). *Phys. Status Solidi B*, **221**, 597–615.

Kushnir, V. I. & Suvorov, E. V. (1990). *Phys. Status Solidi A*, **122**, 391–404.

Laue, M. von (1931). *Ergeb. Exakt. Naturwiss.* **10**, 133–158.

Liss, K. D., Hock, R., Gomm, M., Waibel, B., Magerl, A., Krisch, M. & Tucoulou, R. (2000). *Nature (London)*, **404**, 371–373.

Shvyd'ko, Yu. V. (2004). *X-ray Optics.* Berlin: Springer-Verlag.

Shvyd'ko, Yu. V., Gerdau, E., Jaschke, J., Leupold, O., Lucht, M. & Rüter, H. D. (1998). *Phys. Rev. B*, **57**, 4968–4971.

Shvyd'ko, Yu. V., Lerche, M., Wille, H.-C., Gerdau, E., Lucht, M., Rüter, H. D., Alp, E. E. & Khachatryan, R. (2003). *Phys. Rev. Lett.* **90**, 013904.

Stetsko, Yu. P. & Chang, S.-L. (1997). *Acta Cryst.* A**53**, 28–34.

Steyerl, A. & Steinhauser, K.-A. (1979). *Z. Phys.* B**34**, 221–227.

Sutter, J. P., Alp, E. E., Hu, M. Y., Lee, P. L., Sinn, H., Sturhahn, W., Toellner, T. S., Bortel, G. & Colella, R. (2001). *Phys. Rev. B*, **63**, 094111.